

Dimer physics in the Cairo pentagonal antiferromagnet $\text{Bi}_2\text{Fe}_4\text{O}_9$

K. Beauvois,^{1,2,*} V. Simonet,^{2,†} S. Petit,³ J. Robert,² F. Bourdarot,¹ M. Gospodinov,⁴ A. A. Mukhin,⁵ R. Ballou,² V. Skumryev,^{6,7} and E. Ressouche¹

¹*Univ. Grenoble Alpes, CEA, IRIG, MEM, MDN, 38000 Grenoble, France*

²*Institut Néel, CNRS & Univ. Grenoble Alpes, 38000 Grenoble, France*

³*Laboratoire Léon Brillouin, CEA-CNRS, Université Paris-Saclay, CE-Saclay, 91191 Gif sur Yvette, France*

⁴*Institute of Solid State Physics, Bulgarian Academy of Sciences, 1184 Sofia, Bulgaria*

⁵*Prokhorov General Physics Institute, Russian Academy of Sciences, 119991 Moscow, Russia*

⁶*Departament de Física, Universitat Autònoma de Barcelona, 08193 Bellaterra, Barcelona, Spain*

⁷*Institució Catalana de Recerca i Estudis Avançats, 08010 Bellaterra, Barcelona, Spain*

(Dated: June 25, 2022)

A peculiar non collinear magnetic order is known to be stabilized in $\text{Bi}_2\text{Fe}_4\text{O}_9$ materializing a Cairo pentagonal lattice. Using inelastic neutrons scattering, we have measured the spin wave excitations in the magnetically ordered state. The magnetic excitations have been modeled to determine the frustrated superexchange interactions at the origin of the spin arrangement and of a frustration-induced excited state. Moreover, our analysis has revealed a hierarchy in the interactions. This leads to a paramagnetic state (close to the Néel temperature) constituted of strongly coupled antiferromagnetic pairs of spins separated by much less correlated spins. This inhomogeneous spin liquid produces two types of response to an applied magnetic field associated with the two nonequivalent Fe sites, as observed in the magnetization density distributions obtained using polarized neutrons.

Magnetic frustration, expected to occur when all spin pair interactions cannot be simultaneously satisfied, is one of the major ingredients at the origin of the flurry of discoveries in magnetic studies since the last 20 years. One of the basic experimental signature of frustration is the difficulty of a system to order magnetically in spite of significant magnetic interactions, the extreme case being the absence of magnetic order at zero temperature as a consequence of the macroscopic degeneracy of the ground state [1–3]. In materials where the magnetic moments order eventually at finite temperature, this leads in the region above the ordering temperature but well below the temperature characterizing the strength of the interactions, to a classical spin liquid state also called cooperative paramagnetic, where the magnetic moments are highly correlated although fluctuating. This disordered state can sustain well-defined excitations [4] but also zero energy modes, which are the signature of local motions connecting the ground state spin configurations. These modes acquire a gap on entering the ordered phase [5] and are alternatively described in a molecular approach [6]. This rich physics has been well established for triangle based lattices, for instance the Heisenberg kagome antiferromagnet with a unique interaction between all nearest-neighbor spins [4, 7]. Many other exotic manifestations of magnetic frustration have been revealed in quantum systems or with additional ingredients such as strongly anisotropic Hamiltonians [8–10].

Another direction has been opened when we identified an equivalent for the Cairo lattice in the real material $\text{Bi}_2\text{Fe}_4\text{O}_9$ [11]. The Cairo lattice is not based on tri-

angles but on edge-sharing pentagons. It is then still prone to magnetic frustration due to the odd number of bonds in the elementary pentagonal units. This pentagonal lattice has a complex connectivity with threefold and fourfold connected sites at variance with triangle-based lattices, which fosters alternative ways to accommodate frustration. This leads in $\text{Bi}_2\text{Fe}_4\text{O}_9$ to an unconventional ground state consisting in an orthogonal arrangement of the magnetic moments. This classical ground state was also obtained theoretically as well as other interesting phases including, in presence of quantum fluctuations, a resonating valence bond liquid or an orthogonal dimer ground state (valence bond crystal) [12, 13]. The latter recalls the exactly solvable dimer ground state of the Shastry-Sutherland lattice [14] largely investigated for its exotic physics [15, 16]. These findings stimulated further theoretical [17–23] and experimental [24–27] studies on pentagon-based physics, even spreading beyond the field of magnetism. In spite of this interest, an experimental determination of the Hamiltonian of the prototypical material $\text{Bi}_2\text{Fe}_4\text{O}_9$ has never been reported yet that would solely ascertain the crucial influence of frustration on its exotic properties.

In this article, we report the experimental determination of the magnetic interactions in $\text{Bi}_2\text{Fe}_4\text{O}_9$ materializing a Cairo lattice with spins 5/2 using inelastic neutron scattering. A minimum of five exchange interactions allows to account for the magnetic order and for the associated excitations including a quasi-flat mode due to clusters of frustrated spins. We also show the magnetic density maps measured using polarized neutron scattering under magnetic field that reveal an inhomogeneous spin liquid state above the ordering temperature resulting from the hierarchy of interactions.

The unit cell of the orthorhombic oxyde $\text{Bi}_2\text{Fe}_4\text{O}_9$ contains eight magnetic Fe^{3+} ions equally distributed on two

* current address: Institut Laue Langevin, 38000 Grenoble, France; beauvois@ill.fr

† virginie.simonet@neel.cnrs.fr

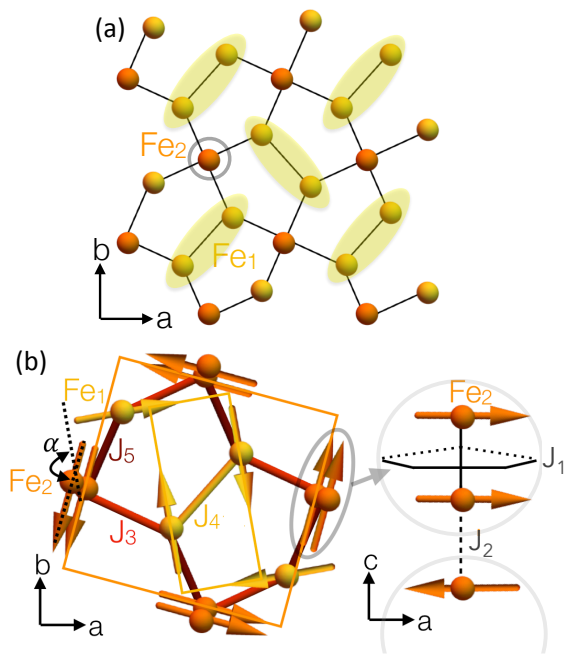


FIG. 1. (a) Projection in the ab plane of the Fe atoms in $\text{Bi}_2\text{Fe}_4\text{O}_9$ that form an analogous to the Cairo pentagonal lattice. The Fe_1 and Fe_2 are in yellow and orange and have a different connectivity. The antiferromagnetically strongly coupled Fe_1 magnetic moments are underlined by the yellow ellipses. (b) Magnetic arrangement stabilized below T_N : the yellow and orange rectangles underline the two sets of orthogonal antiferromagnetic pairs in the ab -plane [11]. The Fe_2 form ferromagnetic pairs sandwiching the Fe_1 planes. The five exchange interactions between the Fe moments in the ab and ac planes are also labeled, the interplane interactions being mediated only via the Fe_2 . The global rotation angle between the two iron sublattices is equal to $\alpha = 155^\circ$.

different Wyckoff sites of the $Pbam$ space group: $4h$ for Fe_1 and $4f$ for Fe_2 . These sites have a different connectivity and different oxygen coordination, tetrahedral for Fe_1 and octahedral for Fe_2 . They form an analogous of the Cairo pentagonal lattice with noticeable differences (see Fig. 1): the site with four-fold connectivity in the perfect lattice is actually constituted by a pair of Fe_2 atoms located below and above the pentagonal plane. The projected lattice in the ab -plane is also slightly distorted compared to the perfect Cairo lattice as far as the bond lengths and bond angles are concerned. The Heisenberg Hamiltonian with only isotropic exchange interactions is a good starting point to describe the magnetic properties of this frustrated lattice of Fe^{3+} ions ($J = S = 5/2$, $L = 0$):

$$\mathcal{H} = \sum_{\langle i,j \rangle} J_{ij} \mathbf{S}_i \cdot \mathbf{S}_j \quad (1)$$

where \mathbf{S}_i is a spin operator and $J_{ij} = J_1$ to J_5 are the five super exchange interactions between pairs of spins, inferred from the structure [11]. There are three exchange

couplings in the ab plane, J_3 , J_4 and J_5 and two additional ones out of the plane of the pentagons, J_1 and J_2 that connect only the stacked Fe_2 (see Fig. 1 (b)). $\text{Bi}_2\text{Fe}_4\text{O}_9$ exhibits below $T_N \sim 240$ K a long-range antiferromagnetic order characterized by a propagation vector $\vec{k} = (1/2, 1/2, 1/2)$. The resulting spin configuration was elucidated by neutron diffraction (see Fig. 1) and is made of two sets of orthogonal pairs of antiferromagnetic spins in the ab -plane corresponding to each Fe site, with a global rotation by an angle $\alpha = 155^\circ$ relative to each other [11]. Despite the deviation of the experimental system from the perfect Cairo lattice, this orthogonal magnetic structure matches the one identified in theoretical studies on the perfect lattice and shown to be rather robust while varying the ratio of the exchange interactions and increasing the quantum fluctuations [13]. This peculiar magnetic structure actually results from both frustration and complex connectivity.

All our experiments were performed on a single crystal of $\text{Bi}_2\text{Fe}_4\text{O}_9$ of dimensions $\sim 2.5 \times 2 \times 1.5 \text{ mm}^3$, grown by the high flux temperature solution method using a flux of Bi_2O_3 . The magnetization distributions were obtained from two neutron scattering experiments performed on the CRG D23 two-axis diffractometer at Institut Laue Langevin (ILL) in its polarized neutron mode, with an incoming neutron wavelength $\lambda = 2.37 \text{ \AA}$ from a graphite-Heusler double monochromator configuration. Measurements were performed with a magnetic field of 6 T applied along the sample c -axis at $T = 250$ K (paramagnetic state) and along the $a - b$ crystallographic direction at $T = 250$ K and 15 K (ordered state) [28]. Inelastic neutron scattering (INS) experiments were performed on the CRG IN22 triple-axis spectrometer at ILL in an orange cryostat at a constant final wave vector $k_f = 2.662 \text{ \AA}^{-1}$, with an energy resolution equal to about 1 meV. The sample was oriented in order to access the (h, h, ℓ) scattering plane.

In order to measure the magnetic excitations, several constant- \mathbf{Q} energy scans have been performed at 1.5 K along the reciprocal space directions $(1/2, 1/2, \ell)$, $(h, h, 0)$ and $(2, 2, \ell)$ sketched in Fig. 2(a). The excitations along $(2, 2, \ell)$ were fitted using the Takin software [29, 30], which includes the spin wave model as input and the instrument resolution (see Fig. 2(b)) [28]. This treatment was necessary to disentangle two overlapping modes. The excitations in the other two directions were simply fitted by the sum of two Lorentz functions:

$$S(\mathbf{Q}, \omega) = bg + A(\omega, T) \left(\frac{1}{(\omega - \epsilon)^2 + \sigma^2} + \frac{1}{(\omega + \epsilon)^2 + \sigma^2} \right) \quad (2)$$

where bg is the background, $A(\omega, T) = (1 + n(\omega, T)Z\omega\sigma/2)$, $n(\omega, T) = 1/(e^{\omega/k_B T} - 1)$ is the Bose factor, Z is the weight of the excitations, ϵ is their energy and σ is the half width at half maximum. The resulting energy position of the excitations is reported as black dots in Figs. 2(f-h). All \mathbf{Q} -scans have been combined into the experimental maps presented in Figs. 2(c-e).

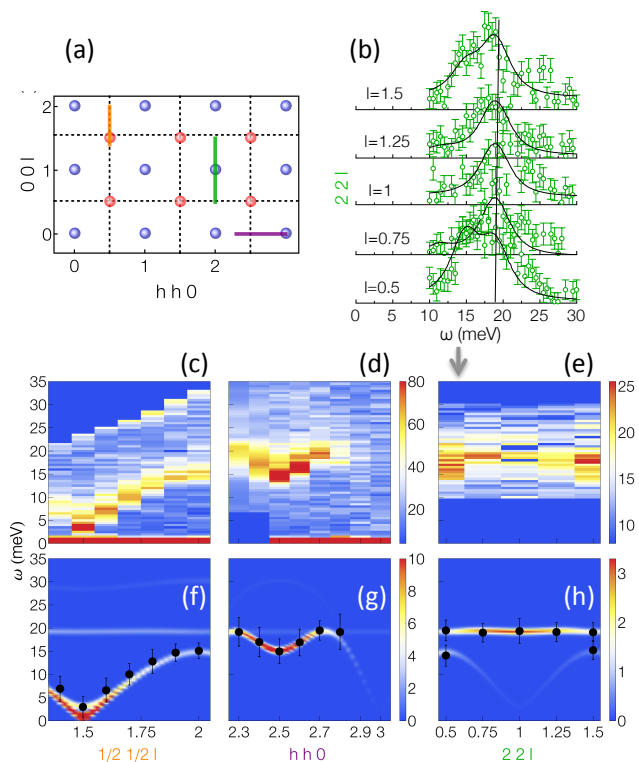


FIG. 2. (a) sketch of the scattering plane (h, h, ℓ) investigated by INS in $\text{Bi}_2\text{Fe}_4\text{O}_9$, with the nuclear (blue spheres) and magnetic (red spheres) Bragg peak positions and the measurement cuts along the $(1/2, 1/2, \ell)$, $(h, h, 0)$ and $(2, 2, \ell)$ reciprocal space directions in orange, purple and green, respectively. (b) Along $(2, 2, \ell)$, series of measured constant- \mathbf{Q} energy scans and fit of the excitations (black lines). Measured (c-e) and calculated (f-h) dynamic structure factor $S(\mathbf{Q}, \omega)$ using the exchange constants of Table I and a small single-ion anisotropy term constraining the spins in the ab -plane. The color scale of the calculations was truncated for the spectra along $(1/2, 1/2, \ell)$, $(h, h, 0)$ in order to emphasize the weaker flat mode along $(2, 2, \ell)$. The width of the calculated excitations was taken as the energy resolution of 1 meV. The black points on top of the calculations give the fitted energy positions of the experimental spin wave dispersion.

The magnetic nature of the excitations have been checked through their temperature dependence. Well defined spin waves are observed, as expected for this ordered compound. An acoustic-like mode emerging from the antiferromagnetic Bragg position $(1/2, 1/2, 1/2)$ is clearly visible, as well as a high-energy branch along $(h, h, 0)$. Additionally, an almost non-dispersive mode located at the energy of about 19 meV is observed along $(2, 2, \ell)$. Note that higher energy modes are inferred from Raman spectroscopy in $\text{Bi}_2\text{Fe}_4\text{O}_9$ with two magnetic excitations identified at the energies 32.2 and 58.5 meV, out of the energy window of our neutron experiments [31].

Our INS measurements were then compared with spin waves calculations performed using the SpinWave software [32, 33] based on the linear spin wave theory us-

ing the Holstein-Primakov formalism [34]. The starting point was the model hamiltonian of Eqn. 1 involving five isotropic super exchange interactions (see Fig. 1). Two additional constrains were used to limit the number of refined parameters. First, it was shown in reference 11 that the rotation angle $\alpha = 155^\circ$ between both iron sublattices is obtained for $J_3/J_5 = 2.15$. A second relation between the exchange interactions was inferred from the Curie-Weiss temperature $\theta_{CW} \approx -1670$ K estimated from magnetic susceptibility measurements [11]. We used the local Weiss molecular field model on the stabilized magnetic structure and the equipartition theorem [35]:

$$2 \times \frac{3}{2} k_B \theta_{CW} = \mathbf{S}_1 \sum_j J_{1j} \langle \mathbf{S}_j \rangle + \mathbf{S}_2 \sum_j J_{2j} \langle \mathbf{S}_j \rangle, \quad (3)$$

where \mathbf{S}_1 (\mathbf{S}_2) is the spin on site Fe_1 (Fe_2). This allowed to further reduce the model to three independent parameters, that were systematically varied in the calculations. We checked the capability of each sets of parameters to reproduce the measured spin waves, as well as the magnetic structure of $\text{Bi}_2\text{Fe}_4\text{O}_9$ through a real-space mean-field energy minimization of the spin configuration. Finally, a model Hamiltonian compatible with the experiments was obtained with the values of the exchange constants given in Table I. The calculated spin waves are displayed in the lower panels of Fig. 2(f-h) and show a very good agreement with the experimental data (black dots and upper panels). The calculations indicate that the spin waves dispersion extends at higher energies up to 80 meV [28], with in particular two zone center modes at the energy positions of the Raman excitations, which further validates our model.

J (meV)	J_1	J_2	J_3	J_4	J_5
IN22	3.7	1.3	6.3	24	2.9

TABLE I. Values of the antiferromagnetic exchange interactions of $\text{Bi}_2\text{Fe}_4\text{O}_9$ deduced from the INS measurements.

Our analysis establishes that all five interactions are antiferromagnetic. Due to the geometry of the pentagonal lattice, this implies competition between the J_3 , J_4 and J_5 interactions within the ab planes leading to the 90° magnetic order previously reported [11]. Moreover, the ferromagnetic Fe_2 pairs of spins sandwiching the pentagonal planes are interacting indirectly through the magnetic paths connecting them to the Fe_1 ions in the ab -planes via J_3 and J_5 . This effective ferromagnetic interaction overcomes the direct superexchange antiferromagnetic interaction J_1 that couples both Fe_2 spins. This results in a peculiar up-up-down-down ordering along the c -axis and leads to a remarkable feature in the magnetic excitations of $\text{Bi}_2\text{Fe}_4\text{O}_9$: a nearly flat optical mode present at around 19 meV, visible in all directions of reciprocal space and associated to these pairs of Fe_2 spins (see Fig 2c). Along $(1/2, 1/2, \ell)$ and $(h, h, 0)$, its intensity is much weaker than that of the low energy modes and was not visible in our experimental data. However, we in-

investigated in purpose the $(2, 2, \ell)$ direction where this mode was strongest in the calculations. We indeed observed the expected signal at 19 meV. This mode can be understood as a strongly frustrated excited state where the deviations out of the local magnetization of the Fe_2 are antiparallel, and moreover almost decoupled from the fluctuations of the four Fe_1 to which they are connected in a triangular pathway. A weak dispersion actually arises from the $J_{1,2}$ couplings in the c direction [28]. However, for the parameters determined in the case of $\text{Bi}_2\text{Fe}_4\text{O}_9$, this dispersion is beyond the instrumental resolution of the experiment.

Also noticeable in Table I is the fact that the J_4 interaction is significantly stronger than the other ones, which is compatible with the 180° super exchange path through the central oxygen ion according to the Goodenough-Kanamori rules [36]. This hierarchy of interactions results in a lattice with dominant pairs of antiferromagnetically coupled spins Fe_1 on almost orthogonal bonds (see Fig. 1a), a picture that is expected to survive above the Néel temperature. Note that the exchange interactions deduced from our spin wave analysis are much stronger than those obtained from ab-initio calculations [37] in the LSDA-U approximation. However, the positive sign of all exchange couplings (antiferromagnetic) and the hierarchy of the interactions are identical in both cases.

T (K)	m (μ_B)	m_{Fe_1} (μ_B)	m_{Fe_2} (μ_B)
250	0.220(5)	0.001(5)	0.045(5)
15	0.263(5)	0.014(8)	0.041(7)

TABLE II. Values of the magnetization measured in $\text{Bi}_2\text{Fe}_4\text{O}_9$ at $T=250$ and 15 K and under a magnetic field $\mu_0 H=6$ T: macroscopic magnetization m per unit cell (2nd column) obtained with an extraction magnetometer with the field direction along $\mathbf{a}-\mathbf{b}$ at 15 K and along $\mathbf{a}-\mathbf{b}$ or \mathbf{c} at 250 K; magnetization per site m_{Fe_1} and m_{Fe_2} (3rd and 4th columns) deduced from the flipping ratio neutron experiments. At $T=15$ K the magnetization density was obtained for $\mathbf{H} \parallel \mathbf{a}-\mathbf{b}$. At $T=250$ K, the magnetization density is the average of the values obtained for $\mathbf{H} \parallel \mathbf{c}$ and $\mathbf{H} \parallel \mathbf{a}-\mathbf{b}$ since the same macroscopic magnetization is measured.

In order to investigate the fingerprint of these Fe_1 dimers in the paramagnetic state, we measured the magnetization distributions under a magnetic field of 6 T with two orientations with respect to the crystallographic axes, as shown in Fig. 3. The magnetization density per site has been extracted from these maps in the dipolar approximation implying a spherical electronic distribution around the atoms. Several fitting processes were performed taking into account the presence of magnetic moments on the iron sites only, or on all the iron, oxygen and bismuth sites. A magnetic contribution can indeed be present on the oxygen atoms and, due to their 6s lone electron pairs, on the Bi atoms. The final averaged magnetization per Fe sites are given in Table II.

Interestingly, in the paramagnetic state (panels (a) and (b)), the two iron sites have radically different behaviors:

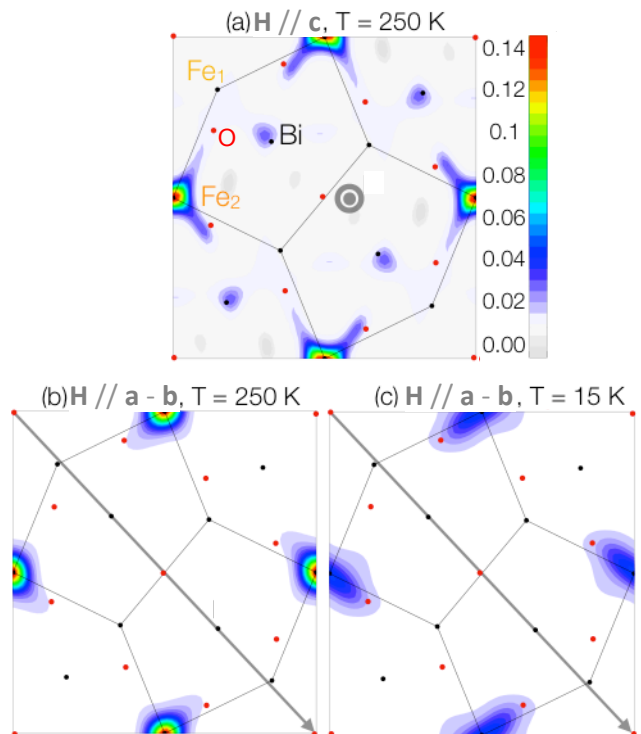


FIG. 3. Spatial distributions of the magnetization of $\text{Bi}_2\text{Fe}_4\text{O}_9$ projected along the \mathbf{c} -axis measured with polarized neutrons under a magnetic field $\mu_0 H = 6$ T applied along \mathbf{c} at $T = 250$ K (a) and along $\mathbf{a}-\mathbf{b}$ at $T = 250$ K (b) and at $T = 15$ K (c).

whereas the Fe_2 ions carry an induced magnetic moment of $0.045(5) \mu_B$ aligned along the field, the induced magnetization on site Fe_1 is vanishingly small (see Table II). This is in contrast with the ordered magnetic moments on both sites refined from previous neutron diffraction experiment below T_N which are rather similar, equal to 3.52 and $3.73 \mu_B$ respectively [11]. Our measurements performed with two different directions of the magnetic field yield the same result, which show that the anisotropy is not responsible for this behavior as expected for Fe^{3+} ions with zero orbital angular momentum. The most noticeable difference between the two maps (a) and (b) is the presence of magnetization density on the Bi sites for $\mathbf{H} \parallel \mathbf{c}$ and not for $\mathbf{H} \parallel \mathbf{a}-\mathbf{b}$. This could be real or an artifact due to an imperfect reconstruction for $\mathbf{H} \parallel \mathbf{c}$ since a smaller number of observations has been used compared to $\mathbf{H} \parallel \mathbf{a}-\mathbf{b}$. The magnetization distribution has also been measured at low temperature (see Fig. 3(c)). A larger field-induced polarization on the Fe_2 compared to the Fe_1 one is actually preserved in the ordered state. As detailed in Table II, the magnetization on the Fe_1 is actually slightly larger at 15 K than at 250 K and also more delocalized [28].

These results point to an original paramagnetic state. A calculation assuming free spins $5/2$ in a 6 T field at 250 K yields a field-polarized magnetization of $0.19 \mu_B$,

that is 4 times larger and almost 200 times larger than the one measured on the Fe_2 and Fe_1 respectively. This suggests that slightly above T_N , the Fe_1 form an assembly of strongly correlated antiferromagnetic dimers in agreement with the dominant J_4 , while the Fe_2 spins are much less correlated. Since the Fe_1 ions form a spin arrangement with great similarities to a Shastry-Sutherland lattice, we suggest that the temperature regime slightly above T_N could be reminiscent of this original physics [14–16]. At higher temperature, the correlations among dimers should vanish, while at lower temperature, correlations involving Fe_2 spins grow, driving the system to the physics of the Cairo pentagonal lattice. Below T_N , the long-range magnetic order is finally triggered by the weakest J_2 interaction, connecting the pentagonal planes. Note that $\text{Bi}_2\text{Fe}_4\text{O}_9$ is not the unique materialization of the Cairo lattice as it is related to a wide family of compounds including the multiferroic RMn_2O_5 (R a rare-earth/Y, Mn occupying the pentagonal lattice) whose complex magnetodielectric phase diagrams could be investigated in the renewed perspective of pentagonal physics [26, 38, 39].

Our neutron scattering investigation of $\text{Bi}_2\text{Fe}_4\text{O}_9$ allowed us to achieve a complete determination of its complex magnetic interactions and to unveil various facets

of unconventional magnetism including frustration and dimer physics, with distinct behaviors associated with the two inequivalent Fe sites of the pentagonal lattice. The Fe_1 ions produce strongly coupled antiferromagnetic pairs of spins dominating the correlated paramagnetic state, whereas in the ordered state, the pairs of Fe_2 spins produce original spin dynamics associated with frustrated excited states coexisting with spin waves. Beyond the canonical examples of frustrated systems like kagome or pyrochlore lattices with first-neighbor interactions, our study discloses novel behaviors that should be more generally observed in materials where the frustration is interlocked with complex connectivity and hierarchical interactions.

ACKNOWLEDGMENTS

We are grateful to J. Debray for the orientation of the sample and the Institut Laue Langevin for providing with the neutrons, and Navid Qureshi for his help in the data analysis. Part of this project was supported by Bulgarian National Science Fund BNSF DN -08/9.

-
- [1] R. Moessner and A. P. Ramirez, *Physics Today* **59**, No 2, 24 (2006).
 - [2] L. Balents, *Nature* **464**, 199 (2010).
 - [3] R. Moessner and K. S. Raman, *Introduction to Frustrated Magnetism*, Vol. 164 (Lacroix, C. and Mendels, P. and Mila, F., Springer, Berlin, 2011).
 - [4] J. Robert, B. Canals, V. Simonet, and R. Ballou, *Phys. Rev. Lett.* **101**, 117207.
 - [5] K. Matan, D. Grohol, D. G. Nocera, T. Yildirim, A. B. Harris, S. H. Lee, S. E. Nagler, and Y. S. Lee, *Phys. Rev. Lett.* **96**, 247201 (2006).
 - [6] K. Tomiyasu, H. Suzuki, M. Toki, S. Itoh, M. Matsuura, N. Aso, and K. Yamada, *Phys. Rev. Lett.* **101**, 177401 (2008).
 - [7] M. E. Zhitomirsky, *Phys. Rev. B* **78**, 094423 (2008).
 - [8] S. T. Bramwell and M. J. P. Gingras, *Science* **294**, 1495 (2001).
 - [9] L. Savary and L. Balents, *Reports on Progress in Physics* **80**, 016502 (2016).
 - [10] K. A., *Annals of Physics* **321**, 2 (2006).
 - [11] E. Ressouche, V. Simonet, B. Canals, M. Gospodinov, and V. Skumryev, *Phys. Rev. Lett.* **103**, 267204 (2009).
 - [12] K. S. Raman, R. Moessner, and S. L. Sondhi, *Phys. Rev. B* **72**, 064413 (2005).
 - [13] I. Rousochatzakis, A. M. Läuchli, and R. Moessner, *Phys. Rev. B* **85**, 104415 (2012).
 - [14] B. S. Shastry and B. Sutherland, *Physica B+C* **108**, 1069 (1981).
 - [15] C. H. Chung, J. B. Marston, and S. Sachdev, *Phys. Rev. B* **64**, 134407 (2001).
 - [16] P. A. McClarty, F. Krüger, T. Guidi, S. F. Parker, K. Refson, A. W. Parker, D. Prabhakaran, and R. Coldea, *Nature Physics* **13**, 736 (2017).
 - [17] F. C. Rodrigues, S. M. de Souza, and O. Rojas, *Annals of Physics* **379**, 1 (2017).
 - [18] V. Urumov, *Journal of Physics A: Mathematical and General* **35**, 7317 (2002).
 - [19] M. Rojas, O. Rojas, and S. M. de Souza, *Phys. Rev. E* **86**, 051116 (2012).
 - [20] H. Nakano, M. Isoda, and T. Sakai, *Journal of the Physical Society of Japan* **83**, 053702 (2014).
 - [21] M. Isoda, H. Nakano, and T. Sakai, *Journal of the Physical Society of Japan* **83**, 084710 (2014).
 - [22] K. Karlova, J. Strecka, and M. L. Lyra, *Phys. Rev. B* **97**, 104407 (2018).
 - [23] A. Ralko, *Phys. Rev. B* **84**, 184434 (2011).
 - [24] A. M. Abakumov, D. Batuk, A. A. Tsirlin, C. Prescher, L. Dubrovinsky, D. V. Sheptyakov, W. Schnelle, J. Hadermann, and G. Van Tendeloo, *Phys. Rev. B* **87**, 024423 (2013).
 - [25] A. A. Tsirlin, I. Rousochatzakis, D. Filimonov, D. Batuk, M. Frontzek, and A. M. Abakumov, *Phys. Rev. B* **96**, 094420 (2017).
 - [26] S. Chattopadhyay, S. Petit, E. Ressouche, S. Raymond, V. Balédent, G. Yahia, W. Peng, J. Robert, M.-B. Lepetit, M. Greenblatt, and P. Foury-Leylekian, *Scientific Reports* **7**, 14506 (2017).
 - [27] J. Cumby, R. D. Bayliss, F. J. Berry, and C. Greaves, *Dalton Trans.* **45**, 11801 (2016).
 - [28] “Details on the magnetization density maps, the spin waves analysis and the quasi-flat excitation can be found in the supplemental material.”
 - [29] T. Weber, R. Georgii, and P. Böni, *SoftwareX* **5**, 121 (2016).

- [30] T. Weber, *SoftwareX* **6**, 148 (2017).
- [31] M. N. Iliev, A. P. Litvinchuk, V. G. Hadjiev, M. M. Gospodinov, V. Skumryev, and E. Ressouche, *Phys. Rev. B* **81**, 024302 (2010).
- [32] S. Petit, *Numerical simulations and magnetism*, Vol. 12 (Collection SFN, 2011) p. 105.
- [33] "<http://www-llb.cea.fr/logicielsllb/SpinWave/SW.html>,".
- [34] T. Holstein and H. Primakoff, *Phys. Rev.* **58**, 1098 (1940).
- [35] R. M. White, *Quantum Theory of Magnetism* (Springer in Solid State Science, 2007).
- [36] G. J. B., *Magnetism and the chemical bond* (John Wiley and Sons, New York, 1963).
- [37] Z. V. Pchelkina and S. V. Streltsov, *Phys. Rev. B* **88**, 054424 (2013).
- [38] P. G. Radaelli and L. C. Chapon, *Journal of Physics: Condensed Matter* **20**, 434213 (2008).
- [39] W. Peng, V. Balédent, C. V. Colin, T. C. Hansen, M. Greenblatt, and P. Foury-Leylekian, *Phys. Rev. B* **99**, 245109 (2019).

Supplemental Material:
Dimer physics in the Cairo pentagonal antiferromagnet $\text{Bi}_2\text{Fe}_4\text{O}_9$

K. Beauvois,^{1,2,*} V. Simonet,² S. Petit,³ J. Robert,² F. Bourdarot,¹ M. Gospodinov,⁴ A. A. Mukhin,⁵ R. Ballou,²
V. Skumryev,^{6,7} and E. Ressouche¹

¹*Univ. Grenoble Alpes, CEA, IRIG, MEM, MDN, 38000 Grenoble, France*

²*Institut Néel, CNRS & Univ. Grenoble Alpes, 38000 Grenoble, France*

³*Laboratoire Léon Brillouin, CEA-CNRS, Université Paris-Saclay, CE-Saclay, 91191 Gif sur Yvette, France*

⁴*Institute of Solid State Physics, Bulgarian Academy of Sciences, 1184 Sofia, Bulgaria*

⁵*Prokhorov General Physics Institute, Russian Academy of Sciences, 119991 Moscow, Russia*

⁶*Departament de Física, Universitat Autònoma de Barcelona, 08193 Bellaterra, Barcelona, Spain*

⁷*Institució Catalana de Recerca i Estudis Avançats, 08010 Bellaterra, Barcelona, Spain*

*Current address: Institut Laue Langevin, 38000 Grenoble, France. Electronic address: beauvois@ill.fr

(Dated: June 25, 2022)

I. MAGNETIZATION DENSITY MAPS

To obtain the magnetization density maps, the flipping ratio method was used. Bragg reflexions were collected up to $\sin\theta/\lambda = 0.36 \text{ \AA}^{-1}$ and the intensities were reduced and corrected for extinction. The polarization for the incident neutron beam was 0.90(1). Accurate magnetic structure factors were extracted from the flipping ratios using the Cambridge Crystallography Subroutine Library [S1]. The magnetization distribution in real space was reconstructed using a uniform prior density and the Maximum of Entropy technique [S2] in order to minimize the noise and truncation effects. 28 and 49 independent magnetic structure factors $F_M(\mathbf{Q})$ were used in the reconstruction for $\mathbf{H} \parallel \mathbf{c}$ and $\mathbf{H} \parallel \mathbf{a} - \mathbf{b}$ respectively, as well as a value of the macroscopic magnetization measured with an extraction magnetometer at Institut Néel.

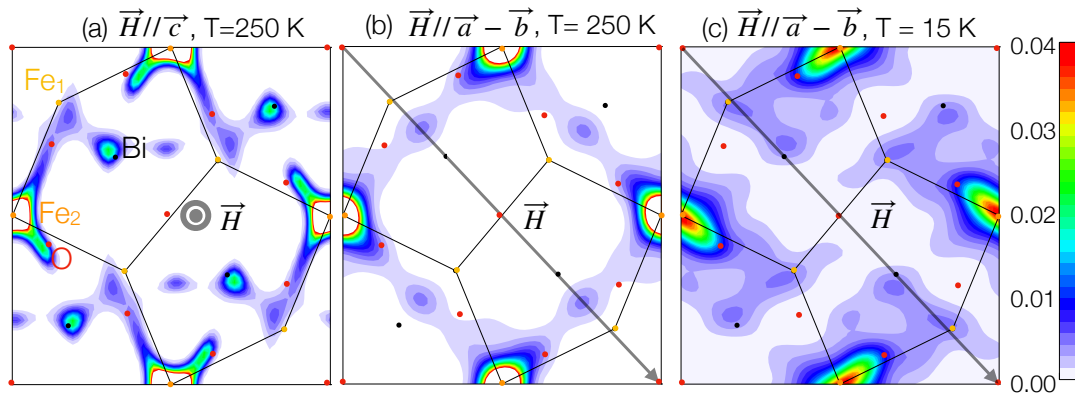


FIG. S1. Same spatial distribution density maps of $\text{Bi}_2\text{Fe}_4\text{O}_9$ as those presented in the main paper (Figure 3) but drawn with a different intensity scale for the magnetization in order to emphasize the weak features. This highlights the delocalization of the magnetization density in the ordered state compared to the paramagnetic state.

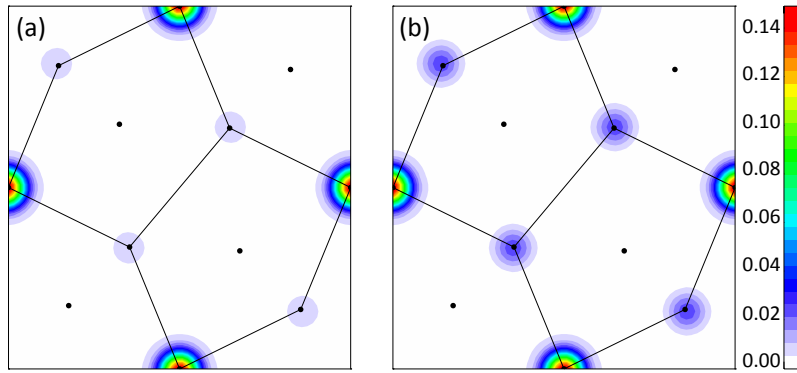


FIG. S2. Calculation of the spatial distribution density maps of $\text{Bi}_2\text{Fe}_4\text{O}_9$ in the dipolar approximation with 0.006 μ_B per Fe_1 and 0.049 μ_B per Fe_2 (a) or 0.016 μ_B per Fe_1 and 0.049 μ_B per Fe_2 (b). These maps have the same intensity scale than those presented in Figure 3 of the main paper and give an insight about the sensitivity of the technique.

II. MAGNETIC EXCITATIONS

A. Inelastic neutron scattering

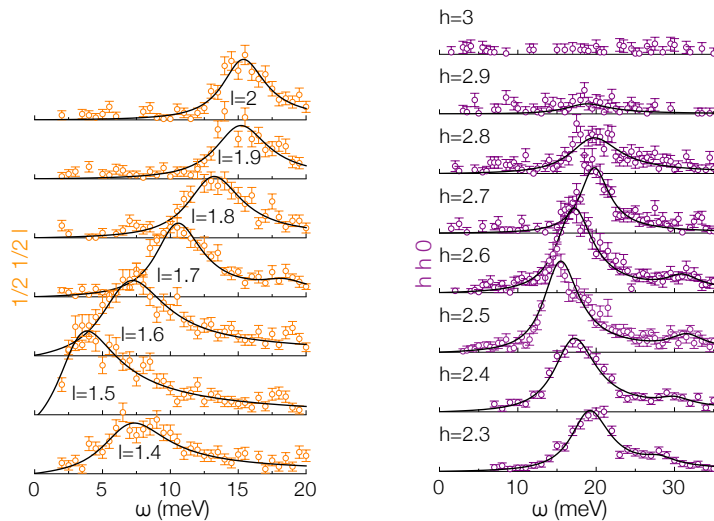


FIG. S3. Series of measured constant- \mathbf{Q} energy scans along $(1/2, 1/2, \ell)$ (orange circles) and $(h, h, 0)$ (purple circles) and fit of the excitations using the model described in the text.

In order to fit the magnetic excitations along $(2, 2, \ell)$, we used the open-source software, Takin, for triple-axis experiments analysis [S3, S4]. We simulated the experimental spectra by convoluting a theoretical dynamical structure factor $S(\mathbf{Q}, \omega)$ model with the instrumental resolution of the IN22 triple axis spectrometer. The resolution function has been calculated using the Popovici algorithm. We used as theoretical model two simple dispersions, one sinusoidal and one flat, for excitations with a lorentzian shape of full width at half maximum equal to 4 meV. The input of the software were the spin wave dispersions and intensities calculated with the SpinWave program allowing a first fit for each constant- \mathbf{Q} ω -scan of the global intensity scale factor and of the offset in ω only. In a second step, all the parameters were let free to vary and a fit of the dispersions, intensities and width of the excitations was performed. This procedure allowed us to distinguish the quasi-flat mode from the lower dispersive mode and to determine precisely its energy position at about 20 meV. The excitations in the other two directions $(1/2, 1/2, \ell)$, $(h, h, 0)$ were simply fitted by the sum of two Lorentz functions as explained in the main paper.

B. Spin waves calculations

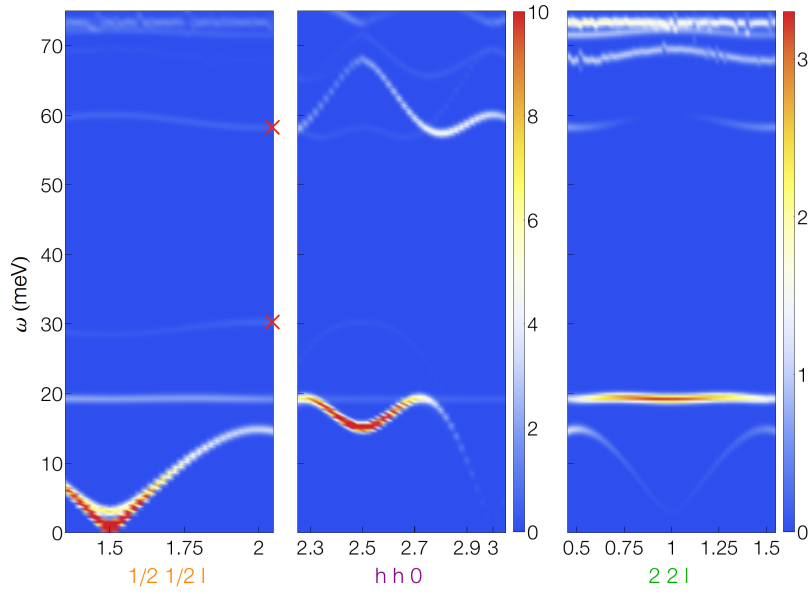


FIG. S4. Calculated dynamic structure factor of $\text{Bi}_2\text{Fe}_4\text{O}_9$ up to 75 meV along the reciprocal space directions $(1/2, 1/2, \ell)$, $(h, h, 0)$ and $(2, 2, \ell)$ showing the complete magnetic spectrum. This was obtained using the SpinWave software [S5, S6] with the five exchange interactions reported in Table I of the main article and a single-ion anisotropy within the ab -plane of 0.03 meV. The red crosses indicate the two magnetic excitations identified in Raman scattering [S7].

III. ADDITIONAL INFORMATION ABOUT THE QUASI FLAT EXCITATIONS

As explained in the main text, the spin excitation spectrum encompasses a peculiar nearly flat optical mode. It involves out of phase deviations of the Fe_2 spins, and remain nearly decoupled from the four Fe_1 to which they are in principle connected in triangular pathways (see Figure S5). Its energy essentially depends on the molecular field due to the Fe_1 as well as on the two exchange couplings J_1 and J_2 . This energy decreases with J_1 since it facilitates the flip of one spin of the Fe_2 pair, but increases with J_2 since the latter favours antiferromagnetic bounds (see Figure S6a). Furthermore, the calculations with the SpinWave software [S5, S6] show that the dispersion of this mode mostly depends on J_2 since this coupling connects Fe_2 pairs along the c axis. For the sake of illustration, Figure S6-b displays the dispersion calculated along $(2, 2, \ell)$ for several values of J_2 ranging from $J_2 = 0.1$ up to $J_2 = 3.1$ meV. Importantly, with increasing J_2 , the bandwidth of the mode increases and finally connects to the acoustic modes stemming from zone centres. Indeed, the localized character (hence the optical trend) of this mode is ensured by small values of J_2 . Figure S6-c shows constant energy cuts (at 5, 10, 15 and 19 meV) across the dispersions. Classical cones are observed stemming from the magnetic Bragg peaks, corresponding to the acoustic modes. Those modes become essentially 1D, forming lines along ℓ . The flat mode has a peculiar dynamical structure factor, which can be deduced from the 19 meV cut. As expected, it essentially depends on ℓ , with stronger intensities at $\ell = 0, 1, 2, \dots$

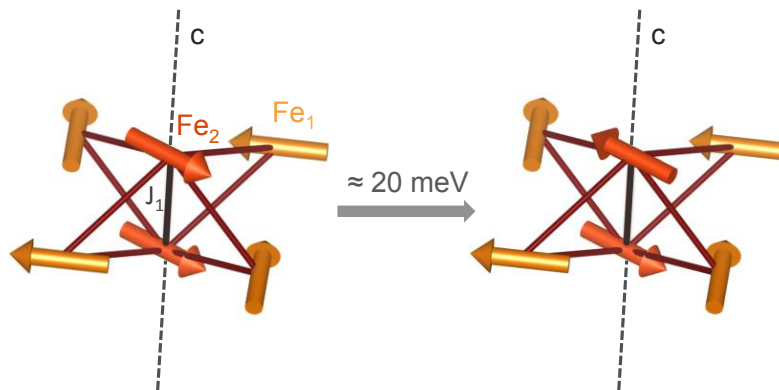


FIG. S5. Schematic description of the frustrated mechanism responsible for the quasi-flat mode observed at 19 meV in the inelastic spectrum. It involves the flip of one Fe_2 spin out of the ferromagnetic pair connected via a triangular exchange path to four Fe_1 neighbors.

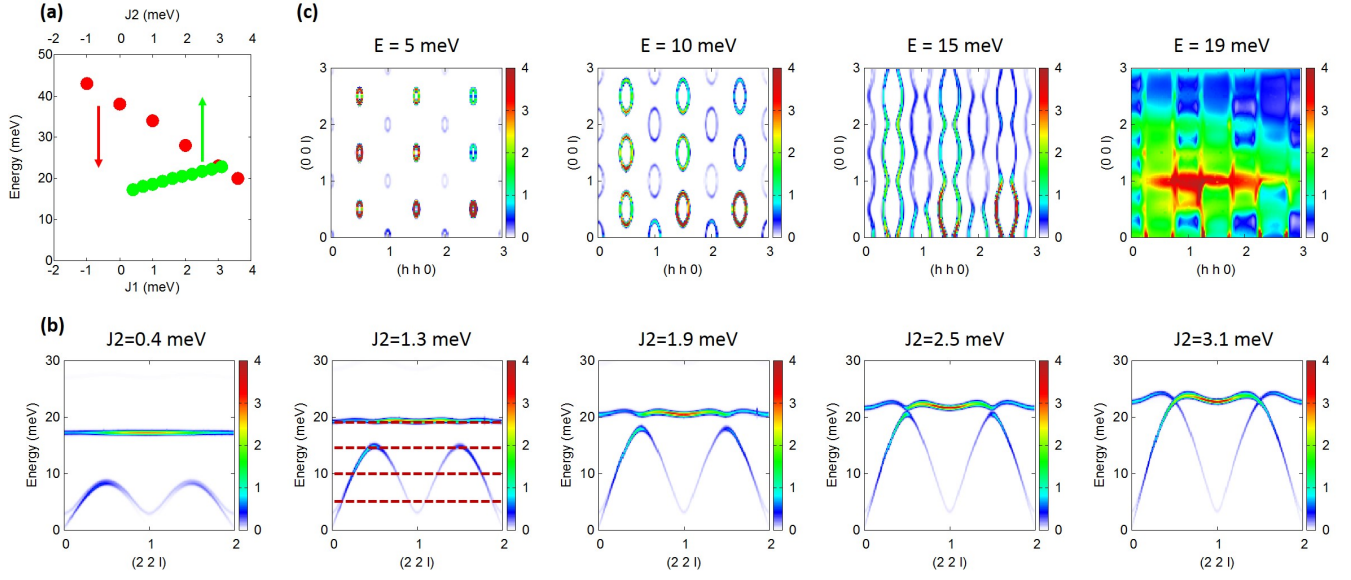


FIG. S6. (a): Dependence of the energy position of the quasi-flat mode with respect to the value of the J_1 (red) and J_2 (green) antiferromagnetic interactions connecting directly the two Fe_2 spins along the \mathbf{c} direction. (b) Dispersion of the spinwaves calculated along $(2, 2, \ell)$ for several values of J_2 . The bandwidth of the flat mode is found to increase with increasing J_2 up to a point where it connects to the acoustic mode. (c) Cuts at various constant energies across the dispersions for $J_2 = 1.3$ meV. The energies are shown as dotted lines on the dispersion along $(2, 2, \ell)$.

-
- [S1] J. C. Matthewman, P. Thompson, and P. J. Brown, *Journal of Applied Crystallography* **15**, 167 (1982).
- [S2] J. Skilling and S. F. Gull, *Maximum Entropy and Bayesian Methods in Inverse Problems* (C.R. Smith and W.T. Grandy Jr., Springer, Dordrecht, 1985) p. 83.
- [S3] T. Weber, R. Georgii, and P. Böni, *SoftwareX* **5**, 121 (2016).
- [S4] T. Weber, *SoftwareX* **6**, 148 (2017).
- [S5] S. Petit, *Numerical simulations and magnetism*, Vol. 12 (Collection SFN, 2011) p. 105.
- [S6] <http://www-llb.cea.fr/logicielsllb/SpinWave/SW.html>
- [S7] M. N. Iliev, A. P. Litvinchuk, V. G. Hadjiev, M. M. Gospodinov, V. Skumryev, and E. Ressouche, *Phys. Rev. B* **81**, 024302 (2010).